Journal of Control, Automation and Electrical Systems
https://doi.org/10.1007/s40313-020-00667-9

Gauss-Newton Algorithm

Predictive Control of Linear Systems with Switched Actuators Subject to Dwell-Time Constraints

Matheus Henrique Marcolino[1] · **Roberto Kawakami Harrop Galvão**[2] · **Karl Heinz Kienitz**[2]

Received: 28 February 2020 / Revised: 5 October 2020 / Accepted: 5 November 2020

Abstract

This paper is concerned with the control of linear systems with switched actuators subject to lower bounds on dwell times. The problem addressed herein consists of driving the system state to a desired periodic trajectory through suitable perturbations in the switching times. For this purpose, a linearization procedure is derived to describe the relationship between the switching-time perturbations and the resulting state trajectory. This procedure allows the constrained predictive control problem to be cast in the form of a convex quadratic program, which is a key contribution of the present work. Simulation examples with single-input and two-input models are presented for illustration. In all cases, the system state is driven to the desired trajectory with satisfaction of the dwell-time constraints on the switched input signal.

Keywords Switched systems · Dwell-time constraints · Predictive control · Periodic trajectories

1 Introduction

Switched control problems involving transitions between two or more subsystems, commutation among different controllers, or discontinuous control actions have been the object of extensive research (Egerstedt et al. 2003; Wu et al. 2013; Liu et al. 2014). In the context of optimal control, difficulties may arise if the problem is subjected to constraints on the minimum dwell time at every switching level. For instance, these constraints must be addressed in the operation of distributed generation systems due to a minimum period of time required to turn on or shut down individual generators (Ferrari-Trecate et al. 2004; Larsen et al. 2013, 2014; Parisio et al. 2014). The operation of power electronic systems may also be subject to time constraints between successive switchings, owing to physical limitations of the semiconductor components (Loxton et al. 2009) as well as the loss of energy caused by high-frequency switching (Arntzen and Maksimovic 1998). In the attitude regulation of rockets or satellites in the upper atmosphere, the use of on/off thrusters may involve dwell-time constraints due to the time required to initialize or extinguish the flow/burn of propellant (Antropov et al. 1999; Rom and Gany 1992).

Optimal control methods which take into account dwell-time constraints typically comprise two stages. Firstly, the original problem is converted into an equivalent constrained nonlinear program, parameterized by the switching times. The second stage consists in obtaining a solution through the use of suitable numerical solvers (Xu and Antsaklis 2004; Loxton et al. 2009; Stellato et al. 2017). However, the resulting optimization problem is not necessarily convex, which may result in difficulties to obtain a numerical solution.

Within this scope, systems with switched actuators can be regarded as a specific type of switched affine systems. As observed recently (Benmiloud et al. 2019), the control literature on this subject has been mostly concerned with driving the state to a neighbourhood of the desired operating point. However, in some applications, the features of the trajectory in this neighbourhood may be of relevance to meet engineering specifications. For example, in the case of attitude regulation with on-off thrusters, the goal consists in achieving a stable periodic motion with suitable ampli-

✉ Matheus Henrique Marcolino
matheus_henrique@unifei.edu.br

Roberto Kawakami Harrop Galvão
kawakami@ita.br

Karl Heinz Kienitz
kienitz@ita.br

[1] Technological Science Institute, Universidade Federal de Itajubá, Rua Irmã Ivone Drummond, 200, Distrito Industrial II, Itabira, Minas Gerais 35903-087, Brazil

[2] Electronics Engineering Division, Instituto Tecnológico de Aeronáutica, Praça Marechal Eduardo Gomes, 50,Vila das Acácias, São José dos Campos, São Paulo 12228-900, Brazil

Published online: 23 November 2020

tude and frequency (Kienitz and Bals 2005; Kienitz 2006). This task can be complicated by the presence of dwell-time constraints, which may be difficult to handle by using standard techniques for stabilization of limit cycles such as the Poincaré map approach (Benmiloud et al. 2019).

In this context, a mixed-integer predictive control approach was proposed in (Vieira 2013), with preliminary results reported in (Vieira et al. 2011). The proposed formulation employed normalized control actions with integer values -1, 0, $+1$, where 0 corresponds to closed thrusters, and -1, $+1$ correspond to thrusters opened in the clockwise or counter-clockwise direction. Dwell-time constraints were imposed by placing restrictions on the minimum number of consecutive equal elements in the discrete-time control sequence. However, although the resulting control law successfully resulted in stable periodic motion, different limit cycles could be reached, depending on the initial state (angular position and velocity) of the system. In fact, one of the main limitations of the proposed formulation was the adoption of a fixed setpoint as the target for the predictive controller, rather than a suitable cyclic trajectory. In subsequent work, Marcolino et al. (2017) managed to characterize families of periodic trajectories which were consistent with the system dynamics and the dwell-time constraints and could thus be used as feasible targets. Nevertheless, the investigation was concerned with the open-loop behaviour of the system and no control law was proposed to actually stabilize the selected target trajectory.

In the more general setting of cyclic switched systems, Patino et al. (2010) presented a two-step procedure to drive the system state to a suitable periodic trajectory around the desired operating point. The first step consisted in determining an optimal limit cycle through the off-line solution of a nonlinear program with constraints on the dwell time at each mode of the switched system. The second step involved the actual online optimization of the switching times. However, the numerical solution of this optimization problem was based on the Gauss-Newton algorithm, and could be too computationally demanding for actual real-time implementation.

With the aim of simplifying the online optimization problem, the present paper proposes a predictive control law that acts through perturbations in the switching times to drive the system state to a pre-selected periodic target trajectory. A linearization procedure is derived to describe the relation between the switching-time perturbations and the state deviation from the target trajectory. As a result, suitable perturbations that satisfy the dwell-time constraints can be determined by solving a convex quadratic programming problem. For illustration, a double integrator, a single-input two-disk-spring model, and a two-input three-disk-spring model are employed.

The remainder of this paper is organized as follows: Sect. 2 states the problem in more detail, introducing the main assumptions and the control task under consideration. The linearization procedure around the target trajectory is presented in Sect. 3. Section 4 casts the constrained predictive control problem in the form of a convex quadratic program. The characterization of the feasibility region for the initial state through computational geometry operations is also discussed. Section 5 presents the simulation examples. Finally, concluding remarks are given in Sect. 6.

2 Statement of the Problem

Consider a plant with continuous-time dynamics described by a model of the form

$$\dot{x}(t) = A_c x(t) + B_c u(t) \tag{1}$$

where $t \in \mathbb{R}$ is the time variable, $x(t) \in \mathbb{R}^n$ is the state vector, $u(t) \in \{-1, 0, 1\}$ is a piecewise-constant control input and $A_c \in \mathbb{R}^{n\times n}$, $B_c \in \mathbb{R}^{n\times 1}$ are matrices with constant coefficients. In what follows, the duration of the time interval between two consecutive switchings of the control is termed *dwell time*.

In line with the assumptions stated by Marcolino et al. (2017), the input signal is subject to the following switching-time constraints:

- direct commutations from -1 to $+1$ and vice versa are not allowed;
- the dwell time at values -1 or $+1$ must be at least $\Delta t_{\text{on,min}}$;
- the dwell time at value 0 must be at least $\Delta t_{\text{off,min}}$,

where $\Delta t_{\text{on,min}} \geq 0$ and $\Delta t_{\text{off,min}} \geq 0$ are given lower bounds on the dwell times.

Let $x_r(t)$ denote a target state trajectory associated to an admissible input signal $u_r(t)$ of the form

$$u_r(t) = u_r(t_{r_i}),\ t_{r_i} \leq t < t_{r_{i+1}}, \forall i \in \mathbb{N} \tag{2}$$

where t_{r_i} is the ith switching time. Both $x_r(t)$ and $u_r(t)$ are assumed to be periodic, with period T. The number of input switchings within one period is denoted by N.

The problem addressed in this paper consists in determining perturbations in the switching times over a period of oscillation, in order to drive the state from an initial point $x(t_0)$ to the target trajectory. More precisely, after an initial input switching at time $t_0 = t_{r_0}$, the perturbed switching times t_i will be given by

$$t_i = t_{r_i} + \delta t_i\ ,\ i = 1, 2, \ldots, N-1 \tag{3}$$

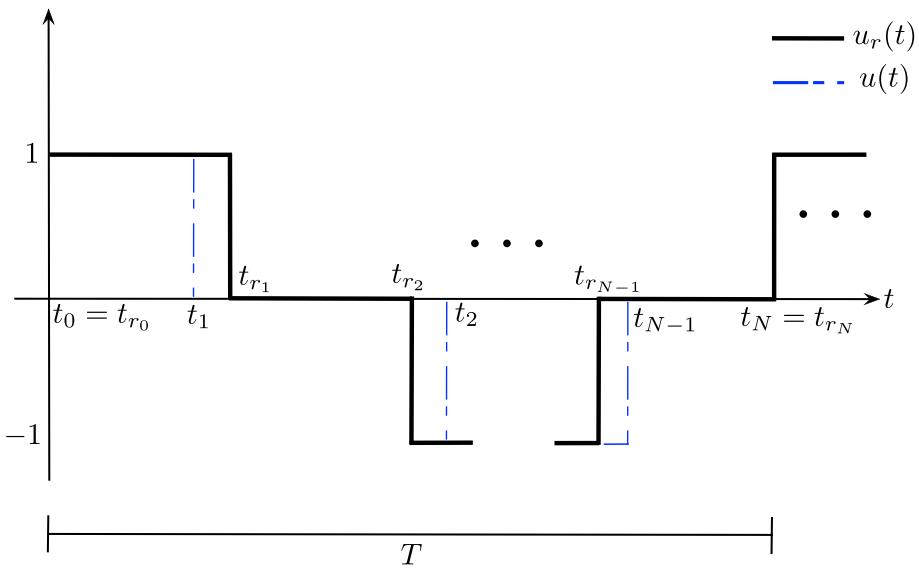

Fig. 1 Input signals $u_r(t)$ and $u(t)$

where $\delta t_1, \delta t_2, \ldots, \delta t_{N-1}$ are the manipulated variables in the control problem. The constraint $t_N = t_{r_N} = t_{r_0} + T$ will be imposed to preserve the oscillation period.

As depicted in Fig. 1, the actual control signal $u(t)$ will be related to $u_r(t)$ as

$$u(t) = u_r(t_{r_i}),\ t_i \leq t < t_{i+1} \tag{4}$$

In order to enforce the lower bounds on the dwell times, the perturbed switching times will be subject to the following constraints:

$$(t_i - t_{i-1}) \geq \Delta t_{i,\min}\,,\ i = 1, 2, \ldots, N \tag{5}$$

with $\Delta t_{i,\min}$ defined as

$$\Delta t_{i,\min} = \begin{cases} \Delta t_{\text{off},\min}, & \text{if } u_r(t_{r_{i-1}}) = 0 \\ \Delta t_{\text{on},\min}, & \text{if } u_r(t_{r_{i-1}}) \neq 0 \end{cases} \tag{6}$$

for $i = 1, 2, \ldots, N$. Now, let

$$\Delta t_{r_i} = t_{r_i} - t_{r_{i-1}}\,,\ i = 1, 2, \ldots, N \tag{7}$$

Since $t_0 = t_{r_0}$, $t_1 = t_{r_1} + \delta t_1$, $\ldots$, $t_{N-1} = t_{r_{N-1}} + \delta t_{N-1}$ and $t_N = t_{r_N}$ the constraints (5) can be restated as

$$\delta t_1 \geq -\Delta t_{r_1} + \Delta t_{1,\min} \tag{8}$$

$$\delta t_i - \delta t_{i-1} \geq -\Delta t_{r_i} + \Delta t_{i,\min}\,,\ i = 2, 3, \ldots, N-1 \tag{9}$$

$$-\delta t_{N-1} \geq -\Delta t_{r_N} + \Delta t_{N,\min} \tag{10}$$

Remark 1: The solution of the state equation (1) at time t_N, starting from the initial condition $x(t_0)$, is of the form

$$x(t_N) = e^{A_c(t_N - t_0)}x(t_0) + \int_{t_0}^{t_N} e^{A_c(t_N-\tau)}B_c u(\tau)\,\mathrm{d}\tau$$

$$= e^{A_c T}x(t_0) + \int_{t_0}^{t_{r_1}+\delta t_1} e^{A_c(t_N-\tau)}B_c u_r(t_{r_0})d\tau + \sum_{i=1}^{N-2}\int_{t_{r_i}+\delta t_i}^{t_{r_{i+1}}+\delta t_{i+1}} e^{A_c(t_N-\tau)}B_c u_r(t_{r_i})d\tau + \int_{t_{r_{N-1}}+\delta t_{N-1}}^{t_N} e^{A_c(t_N-\tau)}B_c u_r(t_{r_{N-1}})d\tau \tag{11}$$

As can be seen, given the target profile $u_r(t)$ for the input signal, the state $x(t_N)$ is a nonlinear function of the switching time perturbations $\delta t_1, \delta t_2, \ldots, \delta t_{N-1}$. In what follows, a linearized model will be derived to describe the relation between these perturbations and the deviation $x(t_N) - x_r(t_N)$ between the plant state and the target trajectory. This linearization procedure is the main result of this paper, as it enables the use of a convex predictive control formulation to drive the state deviation to zero, while enforcing the constraints (8)–(10).

3 Linearization Around the Target Trajectory

3.1 Notation

Let $\delta t \in \mathbb{R}^{N-1}$ be the following vector of switching time perturbations:

$$\delta t = \begin{bmatrix} \delta t_1 \\ \delta t_2 \\ \vdots \\ \delta t_{N-1} \end{bmatrix} \tag{12}$$

The deviation $e(t) \in \mathbb{R}^n$ between the system state and the target trajectory is defined as

$$e(t) = x(t) - x_r(t) \tag{13}$$

The state transition matrices from time t_{r_i} to time t_{r_N} are given by

$$\Phi = e^{A_c(t_{r_N} - t_{r_0})} = e^{A_c T} \tag{14}$$

$$A_i = e^{A_c(t_{r_N} - t_{r_i})}, \ i = 1, 2, \ldots, N-1 \tag{15}$$

The A_i matrices are used to build a matrix $\Gamma \in \mathbb{R}^{n \times (N-1)}$ as

$$\Gamma = -\left[A_1 B_c \Delta u_r(t_{r_1}) \quad A_2 B_c \Delta u_r(t_{r_2}) \cdots \right. \\ \left. \cdots \quad A_{N-1} B_c \Delta u_r(t_{r_{N-1}})\right] \tag{16}$$

where $\Delta u_r(t_{r_i})$ are the following input increments:

$$\Delta u_r(t_{r_i}) = u_r(t_{r_i}) - u_r(t_{r_{i-1}}), \ i = 1, 2, \ldots, N-1 \tag{17}$$

The symbol $\doteq$ will be used to indicate a first-order approximation, as in (Kirk 2004). More specifically, the following approximation will be used:

$$\int_{t_a}^{t_b} e^{-A_c \tau} \mathrm{d}\tau \doteq e^{-A_c t_a}(t_b - t_a) \tag{18}$$

which corresponds to the left-hand rectangle rule for numerical integration if $t_b > t_a$ and to the right-hand rule otherwise (Cantrell (2000), page 101).

3.2 Main Result

The following theorem establishes the model that will be used in the predictive control formulation.

Theorem 1 *A first-order approximation for the relation between the switching-time perturbations and the resulting state deviations is given by*

$$e(t_N) \doteq \Phi e(t_0) + \Gamma \delta t \tag{19}$$

with δt, e, Φ, Γ, defined in (12), (13), (14), (16), respectively.

Proof As stated in Remark 1, the state $x(t_N)$ is given by

$$x(t_N) = e^{A_c(t_N - t_0)} x(t_0) + \int_{t_0}^{t_N} e^{A_c(t_N - \tau)} B_c u(\tau)\, \mathrm{d}\tau \tag{20}$$

This relation also holds for the target trajectory:

$$x_r(t_N) = e^{A_c(t_N - t_0)} x_r(t_0) + \int_{t_0}^{t_N} e^{A_c(t_N - \tau)} B_c u_r(\tau)\, \mathrm{d}\tau \tag{21}$$

From (13), (20) and (21), it follows that

$$e(t_N) = e^{A_c(t_N - t_0)} e(t_0) + \int_{t_0}^{t_N} e^{A_c(t_N - \tau)} B_c [u(\tau) - u_r(\tau)]\mathrm{d}\tau \tag{22}$$

Moreover, since $t_N = t_{r_N} = t_0 + T$, (22) can be rewritten as

$$e(t_N) = e^{A_c T} e(t_0) + \int_{t_0}^{t_{r_N}} e^{A_c(t_{r_N} - \tau)} B_c [u(\tau) - u_r(\tau)]\mathrm{d}\tau \tag{23}$$

In view of the relation between signals $u_r(t)$ and $u(t)$ illustrated in Fig. 1, the integral in (23) can be expressed as

$$\begin{aligned} &\int_{t_0}^{t_{r_N}} e^{A_c(t_{r_N} - \tau)} B_c [u(\tau) - u_r(\tau)]\mathrm{d}\tau \\ &\quad = \sum_{i=1}^{N-1} \int_{t_{r_i}}^{t_i} e^{A_c(t_N - \tau)} B_c [u_r(t_{r_{i-1}}) - u_r(t_{r_i})]\mathrm{d}\tau \\ &\quad = -\sum_{i=1}^{N-1} \left[\int_{t_{r_i}}^{t_i} e^{A_c(t_{r_N} - \tau)} \mathrm{d}\tau\right] B_c \Delta u_r(t_{r_i}) \end{aligned} \tag{24}$$

By using (18) with $t_a = t_{r_i}$ and $t_b = t_i$, the ith integral in (24) can be approximated as

$$\begin{aligned} \int_{t_{r_i}}^{t_i} e^{A_c(t_{r_N} - \tau)} \mathrm{d}\tau &= e^{A_c t_{r_N}} \int_{t_{r_i}}^{t_i} e^{-A_c \tau} \mathrm{d}\tau \\ &\doteq e^{A_c t_{r_N}} e^{-A_c t_{r_i}} (t_i - t_{r_i}) = A_i \delta t_i \end{aligned} \tag{25}$$

with δt_i and A_i defined in (3) and (15), respectively.

Finally, from (23), (24) and (25), it follows that

$$e(t_N) \doteq e^{A_c T} e(t_0) - \sum_{i=1}^{N-1} A_i B_c \Delta u_r(t_{r_i}) \delta t_i \tag{26}$$

which corresponds to (19), with δt, Φ, and Γ given by (12), (14), and (16), respectively. □

In what follows, the approximation (19) is denoted by $\hat{e}(t_N|t_0)$, i.e.

$$\hat{e}(t_N|t_0) = \Phi e(t_0) + \Gamma \delta t \tag{27}$$

Since the plant model (1) is time-invariant, equation (27) can also be used to describe the propagation of the state deviation over subsequent oscillation cycles. More precisely, by using the discrete index $[k]$ to indicate the initial time of the kth oscillation cycle, (27) can be reformulated as

$$\hat{e}[k+1|k] = \Phi e[k] + \Gamma \delta t[k] \tag{28}$$

where $e[k]=e(kT)$ and $\delta t[k]=\left[\,\delta t_1[k]\ \delta t_2[k]\ \cdots\ \delta t_{N-1}[k]\,\right]^T$ is a column vector comprising the switching-time perturbations over this cycle. The hat symbol ($\hat{}$) and the $|k$ notation are used to indicated that $\hat{e}[k+1|k]$ is the predicted value of $e[k+1]$, which depends on $e[k]$ and $\delta t[k]$ through (28).

Remark 2 (Multiple inputs): In the case of plants with multiple inputs $u_1(t), u_2(t), \ldots, u_m(t)$, the continuous-time model (1) becomes

$$\dot{x}(t) = A_c x(t) + \sum_{l=1}^{m} B_{c_l} u_l(t) \tag{29}$$

with $B_{c_l} \in \mathbb{R}^{n\times 1}$. The switching times $t_{l,i}$ and $t_{r_{l,i}}$ of the lth input $u_l(t)$ and its target profile $u_{r_l}(t)$ are related as

$$t_{l,i} = t_{r_{l,i}} + \delta t_{l,i}$$

for $l = 1, 2, \ldots, m$, $i = 1, 2, \ldots, N-1$, with $t_{l,0} = t_{r_{l,0}} = t_{r_0}$ and $t_{l,N} = t_{r_{l,N}} = t_{r_N}$ for all l. A development similar to that employed in the proof of Theorem 1 leads to

$$e(t_N) = e^{A_c T} e(t_0) - \sum_{l=1}^{m}\sum_{i=1}^{N-1}\left[\int_{t_{r_{l,i}}}^{t_{l,i}} e^{A_c(t_{r_{l_N}}-\tau)}\mathrm{d}\tau\right] B_{c_l}\Delta u_{r_l}(t_{r_{l,i}}) \tag{30}$$

By using the approximation (25) with each integral in (30), one arrives at a linearized model of the form (28), with $\delta t \in \mathbb{R}^{m(N-1)}$ given by

$$\delta t = [\delta t_{1,1}\cdots\delta t_{1,N-1}\ \delta t_{2,1}\cdots\delta t_{2,N-1}\cdots\delta t_{m,N-1}]^T \tag{31}$$

Matrix $\Phi \in \mathbb{R}^{n\times n}$ is obtained as in (14) and matrix $\Gamma \in \mathbb{R}^{n\times m(N-1)}$ is arranged as $\Gamma = [\Gamma_1\ \cdots \Gamma_m]$, where

$$\Gamma_l = -\left[A_{l,1}B_{c_l}\Delta u_{r_l}(t_{r_{l,1}})\quad A_{l,2}B_{c_l}\Delta u_{r_l}(t_{r_{l,2}})\ \cdots\ \cdots\ A_{l,N-1}B_{c_l}\Delta u_{r_l}(t_{r_{l,N-1}})\right] \tag{32}$$

with

$$A_{l,i} = e^{A_c(t_{r_N}-t_{r_{l,i}})} \tag{33}$$

and

$$\Delta u_{r_l}(t_{r_{l,i}}) = u_{r_l}(t_{r_{l,i}}) - u_{r_l}(t_{r_{l,i-1}}) \tag{34}$$

for $l = 1, 2, \ldots, m$, $i = 1, 2, \ldots, N-1$.

4 Predictive Control Formulation

The problem addressed herein consists in determining suitable perturbations in the switching times of the input signal in order to drive the state deviation $e[k]$ to zero asymptotically. As a result, the state $x[k]$ will be driven to the target point $x_r(t_0) = x_r(t_N)$.

For this purpose, the discrete-time model (28) derived in the previous section is employed within a predictive control framework. The cost function to be minimized at the beginning of the kth oscillation cycle is chosen as

$$J = ||\hat{e}[k+N_p|k]||^2_{P_f} + \sum_{j=1}^{N_p} ||\hat{e}[k+j|k]||^2_Q + ||\hat{\delta t}[k+j-1|k]||^2_R \tag{35}$$

where $Q = Q^T \in \mathbb{R}^{n\times n}$, $R = R^T \in \mathbb{R}^{(N-1)\times(N-1)}$, $P_f = P_f^T \in \mathbb{R}^{n\times n}$ are positive-definite weight matrices. Following standard predictive control notation, the hat and $[\cdot|k]$ symbols are used to indicate that $\hat{\delta t}[k|k]$, $\hat{\delta t}[k+1|k]$, $\ldots$, $\hat{\delta t}[k+N_p-1|k]$ is a sequence of manipulated vectors which are to be optimized over a prediction horizon spanning N_p oscillation cycles. The relation between these manipulated vectors and the predicted state deviations is given by

$$\hat{e}[k|k] = e[k] \tag{36}$$

$$\hat{e}[k+j|k] = \Phi\hat{e}[k+j-1|k] + \Gamma\hat{\delta t}[k+j-1|k], \quad j = 1, 2, \ldots, N_p \tag{37}$$

In order to enforce (8)–(10) at each oscillation cycle, the following constraints will be imposed:

$$L\hat{\delta t}[k+j-1|k] \geq c, \quad j = 1, 2, \ldots, N_p \tag{38}$$

with $L \in \mathbb{R}^{N\times(N-1)}$ and $c \in \mathbb{R}^N$ given by

$$L = \begin{bmatrix} 1 & 0 & 0 & \cdots & 0 & 0 \\ -1 & 1 & 0 & \cdots & 0 & 0 \\ \vdots & \vdots & \vdots & \ddots & \vdots & \vdots \\ 0 & 0 & 0 & \cdots & -1 & 1 \\ 0 & 0 & 0 & \cdots & 0 & -1 \end{bmatrix}, \quad c = \begin{bmatrix} -\Delta t_{r_1} + \Delta t_{1,\min} \\ -\Delta t_{r_2} + \Delta t_{2,\min} \\ \vdots \\ -\Delta t_{r_{N-1}} + \Delta t_{N-1,\min} \\ -\Delta t_{r_N} + \Delta t_{N,\min} \end{bmatrix} \tag{39}$$

Moreover, nominal stability for the closed-loop system can be obtained by imposing a constraint of the form

$$\hat{e}[k+N_p|k] \in \mathbb{E}_f \tag{40}$$

and choosing a suitable terminal set $\mathbb{E}_f$ and terminal weight matrix P_f. In line with the so-called dual-mode predictive control approach (Rossiter 2003), $\mathbb{E}_f$ will be the maximal admissible set with respect to the constraints (43) under a stabilizing terminal control law of the form $\delta t[k] = -Ke[k]$. The gain $K \in \mathbb{R}^{p\times n}$ is obtained as the solution of an infinite-horizon linear-quadratic regulator problem with matrices Q and R employed as cost weights for the state and the control, respectively. As a result, the terminal set $\mathbb{E}_f$ is defined as the intersection of a finite number of half-spaces, i.e. the constraint (40) can be restated in the form

$$S_f \hat{e}[k+N_p|k] \leq b_f \tag{41}$$

with a matrix S_f and a column vector b_f of suitable dimensions (Gilbert and Tan 1991). Finally, the terminal cost matrix P_f is obtained by solving the following Lyapunov equation:

$$\bar{\Phi}^T P_f \bar{\Phi} - P_f + \bar{\Phi}^T Q \bar{\Phi} + K^T R K = 0 \tag{42}$$

where $\bar{\Phi} = \Phi - \Gamma K$.

The minimization of the cost (35) subject to (36), (37), (43) and (41) is a quadratic program, which can be solved by using efficient convex optimization methods (Maciejowski 2002). The control law is implemented as $\delta t[k] = \hat{\delta t}^*[k|k]$, where * denotes the optimal solution. A proof of nominal stability for the resulting closed-loop system can be found in (Rossiter 2003). A concise presentation is provided in "Appendix B" of (Rossi et al. 2019).

The feasibility region $\mathcal{D} \subset \mathbb{R}^n$ is defined as the set of state deviations $e[k]$ for which the constraints of the optimization problem can be satisfied by some choice of $\hat{\delta t}[k+j-1|k]$, $j = 1, 2, \ldots, N_p$. The characterization of $\mathcal{D}$ can be carried out by using computational geometry operations, as described in "Appendix A" at the end of this paper.

Remark 3: In the case of a system with m inputs as in Remark 2, the cost function can still be chosen as (35), with $\hat{\delta t}[k+j-1|k] \in \mathbb{R}^{m(N-1)}$ and $R = R^T \in \mathbb{R}^{m(N-1)\times m(N-1)}$. The constraints to be enforced at each oscillation cycle become

$$\underline{L}\hat{\delta t}[k+j-1|k] \geq \underline{c}, \quad j = 1, 2, \ldots, N_p \tag{43}$$

with $\underline{L} \in \mathbb{R}^{mN\times m(N-1)}$ and $\underline{c} \in \mathbb{R}^{mN}$ given by

$$\underline{L} = \begin{bmatrix} L & 0 & \cdots & 0 \\ 0 & L & \cdots & 0 \\ \vdots & \vdots & \ddots & \vdots \\ 0 & 0 & \cdots & L \end{bmatrix}, \quad \underline{c} = \begin{bmatrix} -\Delta t_{r_{1,1}} + \Delta t_{1,1,\min} \\ \vdots \\ -\Delta t_{r_{1,N}} + \Delta t_{1,N,\min} \\ -\Delta t_{r_{2,1}} + \Delta t_{2,1,\min} \\ \vdots \\ -\Delta t_{r_{m,N}} + \Delta t_{m,N,\min} \end{bmatrix} \tag{44}$$

where $\Delta t_{r_{l,i}} = t_{r_{l,i}} - t_{r_{l,i-1}}$ and $\Delta t_{l,i,\min}$ is the lower bound on $t_{l,i} - t_{l,i-1}$.

Diferença 'interior-point-convex' p/ 'active-set'

5 Examples

The results presented herein were obtained by using the interior-point-convex solver of the MATLAB Optimization Toolbox™ to solve the quadratic program described in Sect. 4. The Multi-Parametric Toolbox developed by Herceg et al. (2013) was employed to carry out the geometrical operations involved in the determination of the feasibility region $\mathcal{D}$.

5.1 Double Integrator

This first example is concerned with a double integrator model of the form (1), with

$$A_c = \begin{bmatrix} 0 & 1 \\ 0 & 0 \end{bmatrix}, \quad B_c = \begin{bmatrix} 0 \\ 1 \end{bmatrix}. \tag{45}$$

The double integrator is a canonical example, which has often been used to illustrate the application of novel control techniques (Vieira et al. 2011; Gustafsson 1996; Sun et al. 2017). The states x_1, x_2 and the control input u can be interpreted as position, velocity and acceleration variables for either translational or rotational motion (Bernstein 2009). Herein, these quantities, as well as the time variable, are assumed to be normalized and thus their values will be dimensionless.

Marcolino et al. (2017) employed this model to illustrate the search for periodic trajectories subject to switching-time constraints on the input signal. Figure 2a depicts an example of an input signal $u_r(t)$ with $t_0 = 0$, period $T = 6$ and $N = 4$ switching times. The associated state trajectory $x_r(t)$, starting from $x_r(t_0) = [-0.5 \quad -1]^T$ is presented in Fig. 2b (solid line). These input and state profiles will be used as targets for the controller.

The dashed line in Fig. 2b depicts the result of an open-loop simulation starting from $x(t_0) = [-0.5 \quad -0.5]^T$ with no perturbations in the switching times. As can be seen, the target trajectory is open-loop unstable, in the sense that the

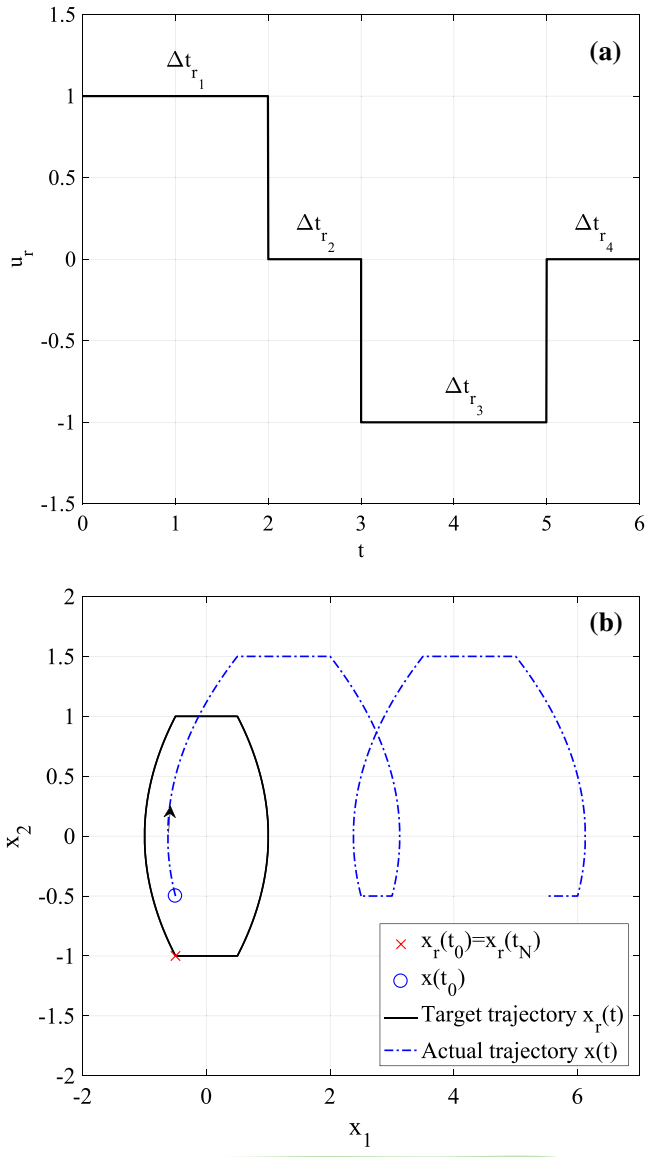

Fig. 2 **a** Target input signal $u_r(t)$, with $\Delta t_{r_1} = 2$, $\Delta t_{r_2} = 1$, $\Delta t_{r_3} = 2$, and $\Delta t_{r_4} = 1$. **b** Target state trajectory $x_r(t)$ and open-loop simulation result $x(t)$

state drifts away if no perturbations on the switching times are applied. In what follows, the proposed predictive control method will be employed to stabilize the target trajectory. To illustrate the enforcement of dwell-time constraints, the lower bounds on the "on" and "off" times for the input signal will be set to $\Delta t_{\text{on,min}} = 1.625$ and $\Delta t_{\text{off,min}} = 0.625$.

Figure 3 presents the feasibility region $\mathcal{D}$ for three different prediction horizons ($N_p = 1$, $N_p = 2$, and $N_p = 3$). Using a larger prediction horizon leads to an enlargement of the feasibility region, which enables the use of the predictive control law with initial conditions $x(t_0)$ farther from the target $x_r(t_0)$. However, this enlargement comes at the cost of greater computational effort for the calculation of the optimal control actions, owing to the larger number of variables in the quadratic program to be solved.

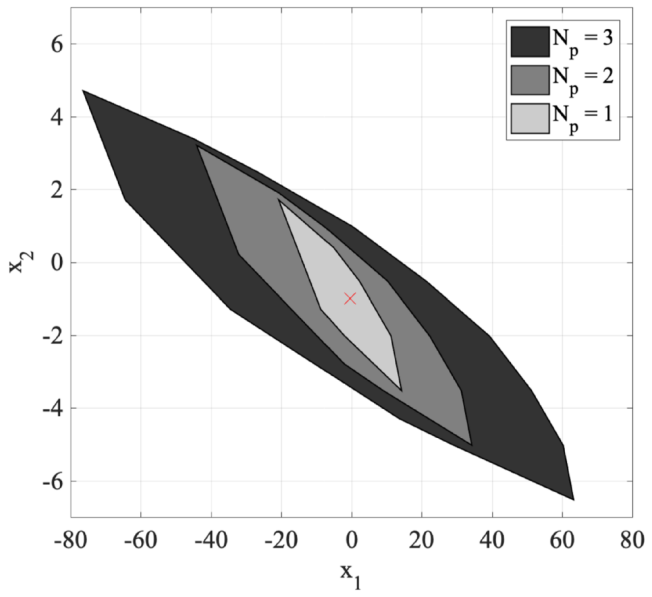

Fig. 3 Feasibility regions for different prediction horizons N_p. The cross ($\times$) marker indicates the target point $x_r(t_0) = x_r(t_N)$

For illustration, a predictive controller was implemented with $N_p = 1$, unit weights for the state and control (i.e. $Q = I$, $R = I$) and P_f calculated from (42). Figure 4a presents the result of a closed-loop simulation starting from $x(t_0) = [-5.1\ 0.4]^T$, which corresponds to a point in the boundary of the feasibility region associated to $N_p = 1$. The inset in Fig. 4a presents an enlarged view around the target point $x_r(t_0) = x_r(t_N)$, indicated by a cross marker $\times$. As can be seen, the state moves progressively closer to the target point at the end of the oscillation cycles. As a result, the difference between the actual trajectory $x(t)$ and the target trajectory $x_r(t)$ is almost imperceptible after the second cycle. A similar behaviour is observed in the input signal shown in Fig. 4b. Moreover, the dwell-time constraints were properly enforced, as shown in Table 1. This table presents the dwell times corresponding to the four segments of the input signal in the first three oscillation cycles. In line with the constraints imposed in the optimization, all dwell times were larger or equal to their respective lower bounds.

5.2 Two-Disk-Spring System

Consider the two-disk-spring system with thruster actuators depicted in Fig. 5. This simplified arrangement is aimed at representing the rotational control of a flexible structure with one rigid-body mode and one torsional mode.

The system dynamics can be described by a model of the form (1), with state $x = \left[\theta_1\ \theta_2\ \dot{\theta}_1\ \dot{\theta}_2\right]^T$ and matrices A_c, B_c

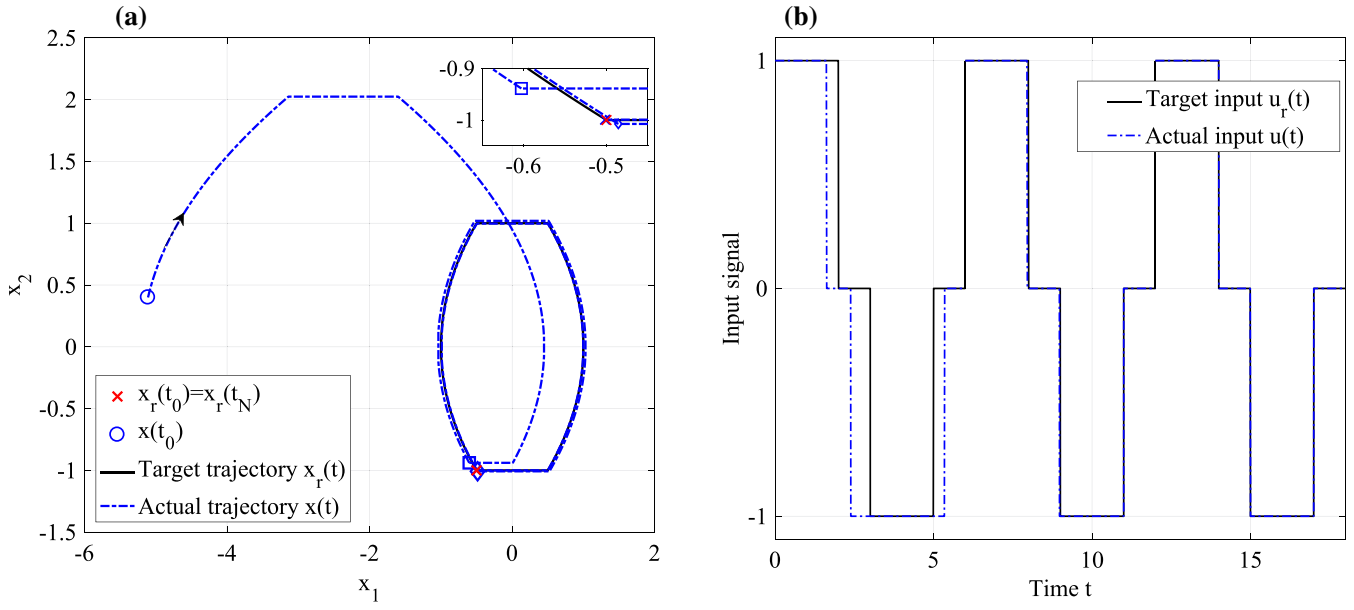

Fig. 4 **a** Target state trajectory $x_r(t)$ and closed-loop simulation result $x(t)$. The square (□) and diamond (◇) markers indicate the actual state after the first and second oscillation cycles, respectively. **b** Target input signal $u_r(t)$ and actual input signal $u(t)$

Table 1 Dwell times and corresponding lower bounds in the first three cycles of the input signal

Lower bound	1st cycle $0 \le t \le 6$	2nd cycle $6 \le t \le 12$	3rd cycle $12 \le t \le 18$
1.625	1.625	1.96	2.005
0.625	0.76	1.01	1.00
1.625	2.96	2.03	2.00
0.625	0.65	1.00	1.00

given by

$$A_c = \begin{bmatrix} 0 & 0 & 1 & 0 \\ 0 & 0 & 0 & 1 \\ -k_s/J_1 & k_s/J_1 & 0 & 0 \\ k_s/J_2 & -k_s/J_2 & 0 & 0 \end{bmatrix}, \; B_c = \begin{bmatrix} 0 \\ 0 \\ 1/J_1 \\ 0 \end{bmatrix}, \quad (46)$$

where k_s is the spring constant, J_1 and J_2 are the moments of inertia of the disks and the input u corresponds to the torque generated by the thrusters (Marcolino 2018). In this example, the physical parameters are assumed to be $k_s = 0.2$ Nm/rad, $J_1 = 5$ kgm^2, $J_2 = 4$ kgm^2, and the possible input values are $u \in \{-1, 0, +1\}$ Nm.

A target trajectory with period $T = 10$ s and $N = 4$ switching times was obtained in (Marcolino 2018), as detailed in "Appendix B". Eight cycles of the target trajectory $x_r(t)$ and the corresponding input signal $u_r(t)$ are presented in Fig. 6 (solid lines), with $t_0 = 0$. The target point for the predictive controller is given by $x_r(t_0) = x_r(t_N) = [0.1533 \text{ rad} \quad -0.0174 \text{ rad} \quad 0.3061 \text{ rad/s} \quad -0.0327 \text{ rad/s}]^T$.

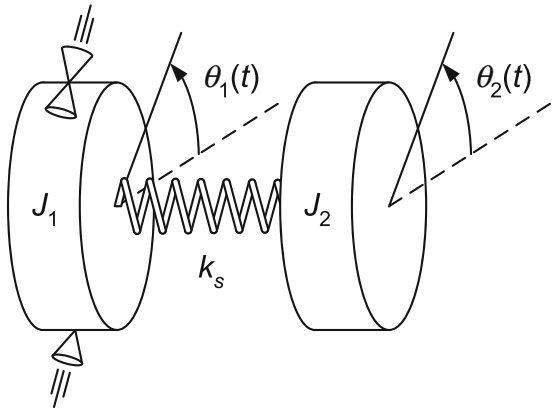

Fig. 5 Two-disk-spring system with thruster actuators

A predictive controller was implemented with $N_p = 5$, unit weights for the state and control (i.e. $Q = I$, $R = 1$) and P_f calculated from (42). The lower bounds on the dwell times for the input signal were set to $\Delta t_{\text{on,min}} = 1.625$ s and $\Delta t_{\text{off,min}} = 0.625$ s. Figure 6 shows the result of a closed-loop simulation starting from $x(t_0) = [0.5 \text{ rad} \quad 0.1 \text{ rad} \quad -0.01 \text{ rad/s} \quad 0 \text{ rad/s}]^T$ and Table 2 presents the dwell times at each segment of the input signal. As can be seen in Table 2, the dwell times were always larger or equal to the corresponding lower bounds, which shows that the constraints were duly enforced. Moreover, the state and control trajectories in Fig. 6 (blue dash-dotted lines) get progressively closer to the target profiles (black solid lines), as desired. However, the state variables still exhibited a considerable difference with respect to the respective targets at the end of the simulation.

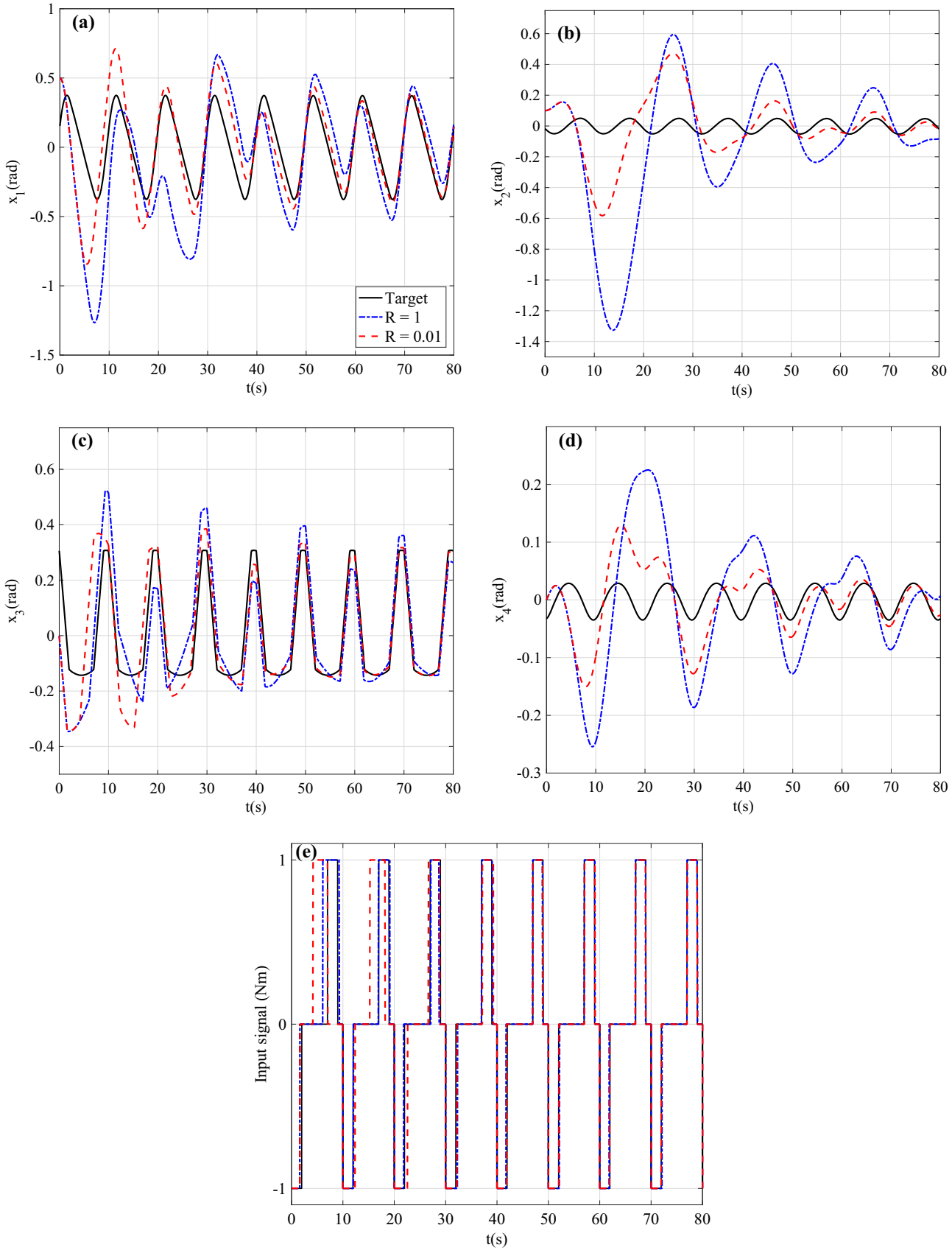

Fig. 6 Two-disk-spring system. Closed-loop simulation results using the predictive controller with control weight $R = 1$ in blue dash-dotted lines and $R = 0.01$ in red dashed lines: **a, b, c, d** state variables and **e** input signal. The black solid line in each plot corresponds to the target profile (Color figure online)

Table 2 Dwell times with $R = 1$ (predictive controller)

Lower bound	1st cycle $0 \le t \le 10$	2nd cycle $10 \le t \le 20$	3rd cycle $20 \le t \le 30$	4th cycle $30 \le t \le 40$	5th cycle $40 \le t \le 50$	6th cycle $50 \le t \le 60$	7th cycle $60 \le t \le 70$	8th cycle $70 \le t \le 80$
1.625	1.625	2.05	1.83	2.32	1.78	2.18	1.85	2.12
0.625	4.47	4.88	5.27	4.73	5.18	4.86	5.11	4.91
1.625	3.23	2.20	1.645	2.07	1.95	2.035	1.99	2.00
0.625	0.68	0.87	1.25	0.885	1.09	0.93	1.05	0.96

In order to obtain faster convergence of the state to the target trajectory, the control weight was reduced from $R = 1$ to $R = 0.01$. Such a reduction places greater emphasis on the reduction of the error in the state variables. As shown in Fig. 6 (red dashed lines), the states at the end of the simulation are now much closer to the respective targets compared to the result for $R = 1$ (blue dash-dotted lines). This improvement was achieved at the cost of a larger deviation of the input signal from the target profile, as can be seen by comparing the simulation results in Fig. 6e. Table 3 shows that some dwell times became closer to the lower bounds, compared to Table 2, but no constraints were violated.

For comparison, a discrete-time linear quadratic regulator (DLQR) was designed by using the dynamic model (28) and an infinite-horizon quadratic cost function with weights $Q = I$ and $R = 0.01$ as in the predictive controller. The resulting control law is given by

$$\delta t[k] = -Ke[k] \tag{47}$$

with gain K calculated as (Lewis and Syrmos 1995):

$$K = (\Gamma^T P \Gamma + R)^{-1} \Gamma^T P \Phi \tag{48}$$

where $P = P^T > 0$ is the solution of the following algebraic Riccati equation:

$$P = \Phi^T \Big[P - P\Gamma \big(\Gamma^T P \Gamma + R\big)^{-1} \Gamma^T P \Big] \Phi + Q \tag{49}$$

As shown in "Appendix C", the infinite-horizon DLQR cost function actually corresponds to the finite-horizon cost (35) employed in the dual-mode predictive control formulation, given that the terminal cost weight P_f is obtained from (42). However, unlike the predictive control strategy, the DLQR control law (47), (48) is not guaranteed to satisfy the dwell-time constraints (8)– (10). Therefore, when the switching-time perturbations $\delta t[k]$ are applied to the plant actuator, a saturation-like phenomenon will occur: A switching will only occur after the minimum dwell time has passed. This saturation was simulated as described in Algorithm 1. It is worth noting that the final switching time t_N may also change as a result.

Algorithm 1: Logic employed in the simulation of the dwell-time constraints in the physical actuator.

Inputs : $t_{r_0}, t_{r_1}, \ldots, t_{r_N}$,
$\Delta t_{1,\min}, \Delta t_{2,\min}, \ldots, \Delta t_{N,\min}$,
DLQR control $\delta t[k] = \begin{bmatrix} \delta t_1 & \delta t_2 & \cdots & \delta t_{N-1} \end{bmatrix}^T$.
Outputs: Switching times $t_1, t_2, \ldots, t_{N-1}, t_N$.
$t_0 \leftarrow t_{r_0}$;
for ($i = 1;\ i < N;\ i = i + 1$)
  if $(t_{r_i} + \delta t_i - t_{i-1}) \ge \Delta t_{i,\min}$ **then**
    $t_i \leftarrow (t_{r_i} + \delta t_i)$;
  else
    $t_i \leftarrow (t_{i-1} + \Delta t_{i,\min})$;
  end

if $(t_{r_N} - t_{N-1}) \ge \Delta t_{N,\min}$ **then**
  $t_N = t_{r_N}$;
else
  $t_N = (t_{N-1} + \Delta t_{N,\min})$
end

Figure 7 present the simulation results. As can be seen, the state trajectories present much larger deviations from the target profile compared to the predictive control results shown in Fig. 6. In fact, the states x_1 and x_2 actually diverge, as shown in the insets of Fig. 7a and b. Table 4 shows that the dwell times resulting from the DLQR control law often violated the constraints and sometimes were even negative, causing the saturation phenomenon previously described. One may argue that the DLQR control is not optimal in this setting, because the switching time constraints are not taken into account in the calculation of the feedback gain K. However, this is precisely the advantage of using a predictive control formulation, namely the possibility of imposing the constraints explicitly in the determination of the optimal control actions.

5.3 Three-Disk-Spring System

In this third example, the system consists of three disks connected by two springs, in a configuration similar to that displayed in Fig. 5. The system dynamics can be described by a model of the form (1), with state $x = \begin{bmatrix} \theta_1 & \theta_2 & \theta_3 & \dot{\theta}_1 & \dot{\theta}_2 & \dot{\theta}_3 \end{bmatrix}^T$ and matrices A_c, B_c given by

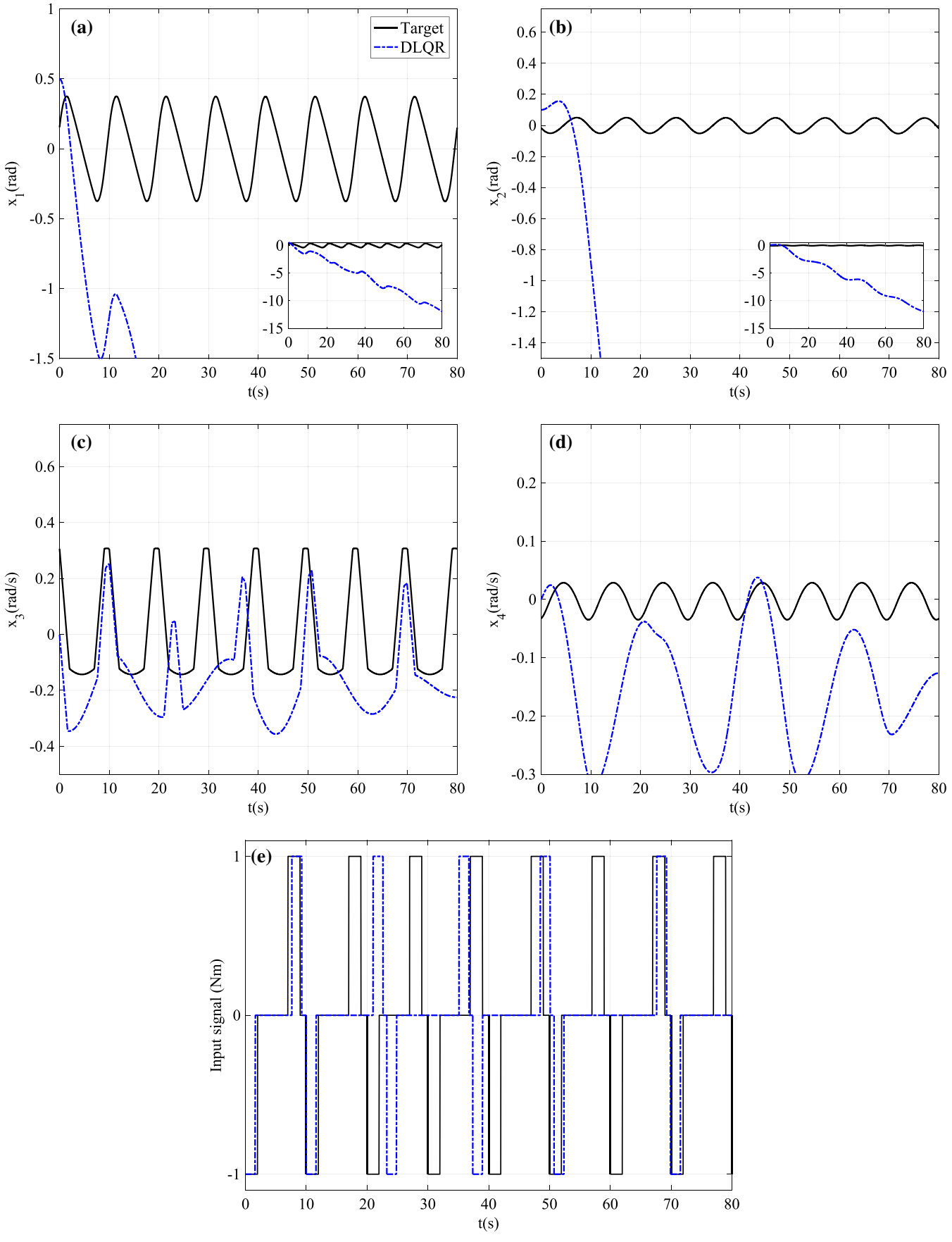

Fig. 7 Two-disk-spring system. Closed-loop simulation results using the DLQR controller with control weight $R = 0.01$: **a, b, c, d** state variables and **e** input signal. The solid and dash-dotted lines in each plot correspond to the target profile and the simulation result, respectively

Table 3 Dwell times with $R = 0.01$ (predictive controller)

Lower bound	1st cycle $0 \le t \le 10$	2nd cycle $10 \le t \le 20$	3rd cycle $20 \le t \le 30$	4th cycle $30 \le t \le 40$	5th cycle $40 \le t \le 50$	6th cycle $50 \le t \le 60$	7th cycle $60 \le t \le 70$	8th cycle $70 \le t \le 80$
1.625	1.625	2.38	2.61	2.20	1.84	2.06	1.96	2.025
0.625	2.57	2.89	4.05	4.96	5.14	4.97	5.03	4.99
1.625	2.87	2.96	2.21	2.135	1.90	2.045	1.97	2.02
0.625	2.94	1.78	1.13	0.70	1.12	0.92	1.05	0.97

Table 4 Dwell times with $R = 0.01$ (DLQR). The value before each slash / is the dwell time yielded by the DLQR calculations. The value after the slash is the actual dwell time resulting from the saturation at the actuator

Lower bound	1st cycle $0 \le t \le 10$	2nd cycle $10 \le t \le 23.2$	3rd cycle $23.2 \le t \le 37.4$	4th cycle $37.4 \le t \le 50.8$	5th cycle $50.8 \le t \le 69.9$	6th cycle $69.9 \le t \le 90.5$	7th cycle $90.5 \le t \le 112.3$	8th cycle $112.3 \le t \le 135.1$
1.625	0.28/1.625	−1.76/1.625	−4.25/1.625	−5.92/1.625	−9.60/1.625	−13.1/1.625	−16.69/1.625	−20.51/1.625
0.625	7.35/6.00	12.75/9.37	16.13/10.26	17.04/9.495	26.50/15.28	31.48/16.76	36.21/17.89	41.105/18.97
1.625	1.53/1.625	−0.82/1.625	−3.03/1.625	−3.92/1.625	−8.34/1.625	−11.36/1.625	−14.33/1.625	−17.45/1.625
0.625	0.84/0.75	−0.18/0.625	1.15/ 0.625	2.80/0.625	1.435/0.625	2.98/0.625	4.81/0.625	6.86/0.625

$$A_c = \begin{bmatrix} 0 & 0 & 0 & 1 & 0 & 0 \\ 0 & 0 & 0 & 0 & 1 & 0 \\ 0 & 0 & 0 & 0 & 0 & 1 \\ -k_{s1}/J_1 & k_{s1}/J_1 & 0 & 0 & 0 & 0 \\ k_{s1}/J_2 & -(k_{s1}+k_{s2})/J_2 & k_{s2}/J_2 & 0 & 0 & 0 \\ 0 & k_{s2}/J_3 & -k_{s2}/J_3 & 0 & 0 & 0 \end{bmatrix},$$

$$B_c = \begin{bmatrix} 0 & 0 \\ 0 & 0 \\ 0 & 0 \\ 1/J_1 & 0 \\ 0 & 0 \\ 0 & 1/J_2 \end{bmatrix} \tag{50}$$

where k_{s1}, k_{s2} are the spring constants, J_1, J_2, J_3 are the moments of inertia of the disks and the input vector $u = [u_1 \quad u_2]^T$ comprises the torques u_1 and u_2 generated by thrusters in the two outer disks. The physical parameters are assumed to be $k_{s1} = 0.2$ Nm/rad, $k_{s2} = 0.1$ Nm/rad, $J_1 = 5$ kgm^2, $J_2 = 4$ kgm^2, $J_3 = 3$ kgm^2 and the possible input values are $u_1, u_2 \in \{-1, 0, +1\}$ Nm.

A target trajectory with period $T = 10$ s and $N = 4$ switching times was obtained by using the procedure described in "Appendix B". As in the previous example, a predictive controller was implemented with $N_p = 5$, $Q = I$, $R = 0.01I$ and P_f calculated from (42). The lower bounds on the dwell times for the input signal were set to $\Delta t_{\text{on,min}} = 1.625$ s and $\Delta t_{\text{off,min}} = 0.625$ s. Figure 8 shows the result of a closed-loop simulation starting from $x(t_0) = [0 \text{ rad} \quad 0.1 \text{ rad} \quad 0 \text{ rad} \quad 0 \text{ rad/s} \quad 0 \text{ rad/s} \quad 0 \text{ rad/s}]^T$. Owing to size limitations, only the angular displacements (x_1, x_2, x_3) and inputs (u_1, u_2) are shown. As can be seen, the trajectories (blue dash-dotted lines) converge to the target profiles (black solid lines), as desired. A DLQR controller was employed for comparison, as in the previous example. Again, the state trajectories (red dashed lines in Fig. 8) exhibit much larger deviations from the target profile compared to the predictive control results.

6 Conclusion

This paper was concerned with a predictive control formulation for systems with switched actuators subject to dwell-time constraints. The goal consisted of driving the system state from an initial point to a desired periodic trajectory, through suitable perturbations in the switching times. For this purpose, a key contribution consisted in the development of a linearized relation between the switching-time perturbations and the deviations of the state from the target trajectory. This linearization procedure allowed the constrained predictive control problem to be cast in the form of a convex quadratic program, which is convenient for implementation purposes.

Simulation examples using a double integrator, a two-disk-spring model and a three-disk-spring model with two inputs were presented to illustrate the use of the proposed framework. The control goals were achieved in that the system state converged to the desired periodic trajectory, with satisfaction of the dwell-time constraints on the switched input signal.

Future work could be concerned with extensions of the proposed method for systems with switching among different sub-systems, such as in DC-DC power converters (Patino et al. 2010). Experimental investigations with laboratory-scale plants could also be pursued.

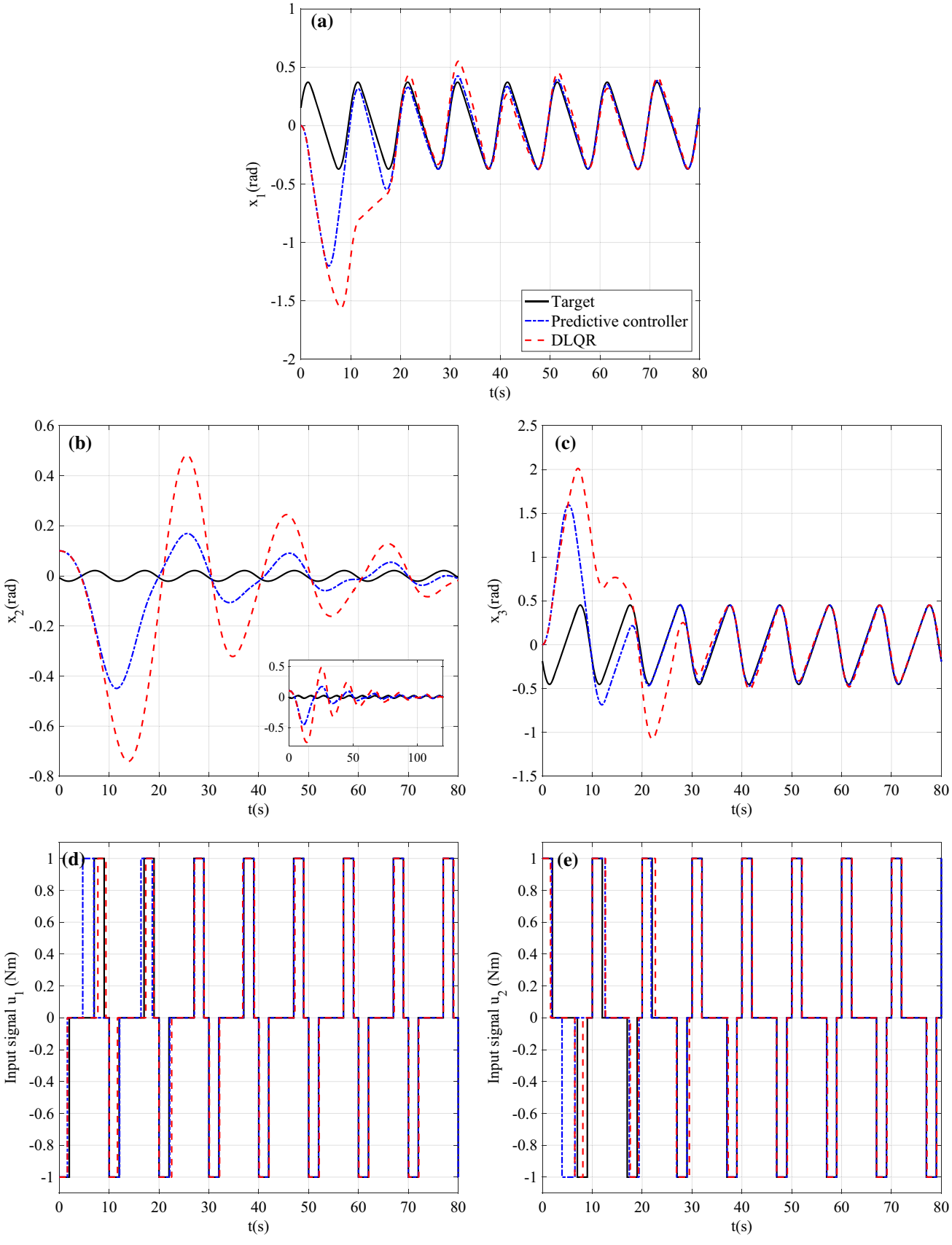

Fig. 8 Three-disk-spring system. Closed-loop simulation results using the predictive controller (blue dash-dotted lines) and the DLQR controller (red dashed lines): **a, b, c** state variables x_1, x_2, x_3 and **d, e** input signals u_1, u_2. The black solid line in each plot corresponds to the target profile (Color figure online)

Acknowledgements This study was financed in part by the Coordenação de Aperfeiçoamento de Pessoal de Nível Superior - Brasil (CAPES) - Finance Code 001 - during the first author's PhD program (Marcolino 2018). The second and third authors acknowledge the support of CNPq (Research Fellowships 303393/2018-1, 306900/2018-1) and FAPESP (Grant 2011/17610-0).

Appendix A

The feasibility region $\mathcal{D} \subset \mathbb{R}^n$ is defined as the set of state deviations $e[k]$ for which the constraints (43) and (41) are feasible, with $\hat{e}[k+N_p|k]$ related to $\hat{\delta t}[k+j-1|k]\,,\ j = 1, 2, \ldots, N_p$ through (36), (37). In order to characterize $\mathcal{D}$ by using computational geometry operations, let $\hat{\boldsymbol{\delta}}\mathbf{t} \in \mathbb{R}^{(N-1)N_p}$ be defined as

$$\hat{\boldsymbol{\delta t}} = \begin{bmatrix} \hat{\delta t}[k|k] \\ \hat{\delta t}[k+1|k] \\ \vdots \\ \hat{\delta t}[k+N_p-1|k] \end{bmatrix} \tag{51}$$

From (36) and (37), it follows that

$$\hat{e}[k+N_p|k] = \Phi^{N_p} e[k] + H_f \hat{\boldsymbol{\delta t}} \tag{52}$$

with $H_f \in \mathbb{R}^{n\times(N-1)N_p}$ given by

$$H_f = \begin{bmatrix} \Phi^{N_p-1}\Gamma & \Phi^{N_p-2}\Gamma & \cdots & \Gamma \end{bmatrix} \tag{53}$$

Therefore, the constraint (41) can be restated as

$$S_f \Phi^{N_p} e[k] + S_f H_f \hat{\boldsymbol{\delta t}} \leq b_f \tag{54}$$

Now, let $\mathbf{L} \in \mathbb{R}^{NN_p\times(N-1)N_p}$ and $\mathbf{c} \in \mathbb{R}^{NN_p}$ be defined as

$$\mathbf{L} = \begin{bmatrix} L & 0 & \cdots & 0 \\ 0 & L & \cdots & 0 \\ \vdots & \vdots & \ddots & \vdots \\ 0 & 0 & \cdots & L \end{bmatrix}, \quad \mathbf{c} = \begin{bmatrix} c \\ c \\ \vdots \\ c \end{bmatrix} \tag{55}$$

The constraint (43) can then be rewritten as

$$\mathbf{L}\hat{\boldsymbol{\delta t}} \geq \mathbf{c} \tag{56}$$

The inequalities (54) and (56) can also be expressed in the following form:

$$\begin{bmatrix} S_f H_f & S_f \Phi^{N_p} \\ -\mathbf{L} & 0 \end{bmatrix} \begin{bmatrix} \hat{\boldsymbol{\delta t}} \\ e[k] \end{bmatrix} \leq \begin{bmatrix} b_f \\ -\mathbf{c} \end{bmatrix} \tag{57}$$

which describes a polyhedron $\mathcal{P} \subset \mathbb{R}^{(N-1)N_p+n}$. The feasibility region $\mathcal{D}$ corresponds to the set of points $e[k]$ for which there exist $\hat{\boldsymbol{\delta t}}$ such that

$$\begin{bmatrix} \hat{\boldsymbol{\delta t}} \\ e[k] \end{bmatrix} \in \mathcal{P} \tag{58}$$

Therefore, $\mathcal{D}$ can be obtained by projecting $\mathcal{P}$ onto the subspace corresponding to the $e[k]$ components.

Appendix B

Consider a state equation of the form

$$\dot{x}_r(t) = A_c x_r(t) + B_c u_r(t) \tag{59}$$

with $x_r(t) \in \mathbb{R}^n$, $u_r(t) \in \mathbb{R}^m$, $A_c \in \mathbb{R}^{n\times n}$ and $B_c \in \mathbb{R}^{n\times m}$. The input signal $u_r(\cdot)$ is assumed to be T-periodic and piecewise constant with N switchings over each period, i.e.

$$u_r(t+T) = u_r(t), \forall t \geq t_{r_0} \tag{60}$$

$$u_r(t) = u_r(t_{r_i}),\ t_{r_i} \leq t < t_{r_{i+1}}\ \forall i \in \mathbb{N} \tag{61}$$

Proposition 1 *The state trajectory $x_r(\cdot)$ starting from $x_r(t_{r_0})$ is T-periodic if and only if the following condition holds:*

$$e^{A_c T} x_r(t_{r_0}) + \int_{t_{r_0}}^{t_{r_0}+T} e^{A_c(t_{r_0}+T-\tau)} B_c u_r(\tau) d\tau = x_r(t_{r_0}) \tag{62}$$

Proof **(Necessity)** If $x_r(\cdot)$ is T-periodic, then

$$x_r(t_{r_0}+T) = x_r(t_{r_0}) \tag{63}$$

The solution of the state equation (59) at time $t_{r_0}+T$ is

$$x_r(t_{r_0}+T) = e^{A_c T} x_r(t_{r_0}) + \int_{t_{r_0}}^{t_{r_0}+T} e^{A_c(t_{r_0}+T-\tau)} B_c u_r(\tau) d\tau \tag{64}$$

From (63) and (64), one arrives at (62), qed.
(Sufficiency) The solution of the state equation (59) at time $t+T$, with $t > t_{r_0}$, is

$$x_r(t+T) = e^{A_c(t+T-t_{r_0})} x_r(t_{r_0}) + \int_{t_{r_0}}^{t+T} e^{A_c(t+T-\tau)} B_c u_r(\tau) d\tau \tag{65}$$

From (62) and (65), it follows that

$$x_r(t+T) = e^{A_c(t-t_{r_0})} \left[x_r(t_{r_0}) - \int_{t_{r_0}}^{t_{r_0}+T} e^{A_c(t_{r_0}+T-\tau)} B_c \right.$$

$$u_r(\tau)d\tau \Big] + \int_{t_{r_0}}^{t+T} e^{A_c(t+T-\tau)} B_c u_r(\tau)d\tau$$
$$= e^{A_c(t-t_{r_0})} x_r(t_{r_0}) + \int_{t_{r_0}+T}^{t+T} e^{A_c(t+T-\tau)} B_c u_r(\tau)d\tau \quad (66)$$

By using a new integration variable $\xi = \tau - T$ and noting that $u_r(\cdot)$ is T-periodic, one can write

$$\int_{t_{r_0}+T}^{t+T} e^{A_c(t+T-\tau)} B_c u_r(\tau)d\tau$$
$$= \int_{t_{r_0}}^{t} e^{A_c(t-\xi)} B_c u_r(\xi+T)d\xi = \int_{t_{r_0}}^{t} e^{A_c(t-\xi)} B_c u_r(\xi)d\xi \quad (67)$$

From (66) and (67), it follows that

$$x_r(t+T) = e^{A_c(t-t_{r_0})} x_r(t_{r_0}) +$$
$$= \int_{t_{r_0}}^{t} e^{A_c(t-\xi)} B_c u_r(\xi)d\xi = x_r(t) \quad (68)$$

which shows that $x_r(\cdot)$ is T-periodic, qed.

□

Remark 1 In view of the piecewise-constant profile (61) of the input $u_r(\cdot)$, condition (62) can also be expressed as

$$(I - e^{A_c T}) x_r(t_{r_0}) = \begin{bmatrix} W_0 & W_1 & \cdots & W_{N-1} \end{bmatrix} \begin{bmatrix} u_r(t_{r_0}) \\ u_r(t_{r_1}) \\ \vdots \\ u_r(t_{r_{N-1}}) \end{bmatrix} \quad (69)$$

where

$$W_i = \int_{t_{r_i}}^{t_{r_{i+1}}} e^{A_c(t_{r_0}+T-\tau)} B_c \, d\tau \;, i = 0, 1, \ldots, N-1 \quad (70)$$

From this point, the following notation will be employed:

$$W = \begin{bmatrix} W_0 & W_1 & \cdots & W_{N-1} \end{bmatrix}, \quad \bar{u}_r = \begin{bmatrix} u_r(t_{r_0}) \\ u_r(t_{r_1}) \\ \vdots \\ u_r(t_{r_{N-1}}) \end{bmatrix} \quad (71)$$

If A_c has one or more eigenvalues at the origin (i.e. if the system has integrating modes) then $(I - e^{A_c T})$ will be rank-deficient. In this case, the vector of input values $\bar{u}_r$ and the initial condition $x_r(t_{r_0})$ will have to satisfy specific conditions derived from (69).

Let $p < n$ be the rank of matrix $(I - e^{A_c T})$. By using a singular value decomposition, one can write

$$(I - e^{A_c T}) = USV^T \quad (72)$$

with $U, S, V \in \mathbb{R}^{n \times n}$ such that $U^T = U^{-1}$, $V^T = V^{-1}$ and

$$S = \begin{bmatrix} S_p & 0_{p\times(n-p)} \\ 0_{(n-p)\times p} & 0_{(n-p)\times(n-p)} \end{bmatrix} \quad (73)$$

where $S_p \in \mathbb{R}^{p \times p}$ is a full-rank diagonal matrix. By using (71) and (72), the identity (69) can be rewritten as

$$W\bar{u}_r = USV^T x_r(t_{r_0}) \quad (74)$$

After multiplying both sides of (74) by U^T, it follows that:

$$U^T W\bar{u}_r = SV^T x_r(t_{r_0}) \quad (75)$$

Let U and V be partitioned as

$$U = \begin{bmatrix} U_1 & U_2 \end{bmatrix} \quad (76)$$
$$V = \begin{bmatrix} V_1 & V_2 \end{bmatrix} \quad (77)$$

where $U_1, V_1 \in \mathbb{R}^{n \times p}$, and $U_2, V_2 \in \mathbb{R}^{n \times (n-p)}$. Then, in view of (73), (75) and (76), it follows that

$$U_2^T W\bar{u}_r = 0_{(n-p)\times 1} \quad (78)$$

which is a constraint that must be satisfied by $\bar{u}_r$.

Assuming that $\bar{u}_r$ satisfies (78), a set of initial conditions $x_r(t_{r_0})$ that satisfy (69) can be parameterized as follows. From (73), (75)-(77), it follows that:

$$S_p V_1^T x_r(t_{r_0}) = U_1^T W\bar{u}_r \quad (79)$$

After multiplying both sides of (79) by S_p^{-1}, one obtains

$$V_1^T x_r(t_{r_0}) = S_p^{-1} U_1^T W\bar{u}_r \quad (80)$$

Therefore, the solutions for $x_r(t_{r_0})$ will be of the form

$$x_r(t_{r_0}) = V_2 z + x_p \quad (81)$$

where $z \in \mathbb{R}^{n-p}$ is a vector of free parameters and x_p is given by

$$x_p = V_1 (V_1^T V_1)^{-1} S_p^{-1} U_1^T W\bar{u}_r \quad (82)$$

Indeed, from (81) and (82), one can write

$$V_1^T x_r(t_{r_0}) = V_1^T V_2 z + V_1^T V_1 (V_1^T V_1)^{-1} S_p^{-1} U_1^T W\bar{u}_r \quad (83)$$

Since the columns of $V = [V_1\ V_2]$ are mutually orthogonal, one has $V_1^T V_2 = 0$, and thus (83) results in (80) for any parameter vector z. Convenient values for z can be chosen in order to obtain a state trajectory with suitable features. In the present work, z was adjusted in order to obtain symmetric oscillations of the angular displacement variables around the origin.

Appendix C

By using predictive control notation, the DLQR cost is expressed as the following infinite-horizon summation:

$$J_{DLQR} = \sum_{j=1}^{\infty} ||\hat{e}[k+j|k]||_Q^2 + ||\hat{\delta t}[k+j-1|k]||_R^2 \quad (84)$$

which is minimized by a state feedback control law of the form

$$\hat{\delta t}[k+j-1|k] = -K\hat{e}[k+j-1|k]\,, \forall j \geq 1 \quad (85)$$

with a constant gain K. The cost J_{DLQR} can be split into two terms as

$$J_{DLQR} = J_f + \sum_{j=1}^{N_p} ||\hat{e}[k+j|k]||_Q^2 + ||\hat{\delta t}[k+j-1|k]||_R^2 \quad (86)$$

where

$$J_f = \sum_{j=1}^{\infty} ||\hat{e}[k+N_p+j|k]||_Q^2 + ||\hat{\delta t}[k+N_p+j-1|k]||_R^2 \quad (87)$$

From (85), it follows that

$$\begin{aligned}\hat{e}[k+j|k] &= \Phi\hat{e}[k+j-1|k] + \Gamma\hat{\delta t}[k+j-1|k] \\ &= (\Phi - \Gamma K)\hat{e}[k+j-1|k] = \bar{\Phi}\hat{e}[k+j-1|k]\end{aligned}$$

and thus

$$\hat{e}[k+N_p+j|k] = \bar{\Phi}^j\hat{e}[k+N_p|k] \quad (88)$$

From (85), (87) and (88), it follows that

$$\begin{aligned}J_f &= \sum_{j=1}^{\infty} ||\bar{\Phi}^j\hat{e}[k+N_p|k]||_Q^2 + ||K\bar{\Phi}^{j-1}\hat{e}[k+N_p|k]||_R^2 \\ &= \hat{e}^T[k+N_p|k]\left[\sum_{j=0}^{\infty}(\bar{\Phi}^T)^j(\bar{\Phi}^T Q\bar{\Phi} + K^T RK)\bar{\Phi}^j\right]\end{aligned}$$

$$\hat{e}[k+N_p|k] \quad (89)$$

Since K is a stabilizing gain, the eigenvalues of $\bar{\Phi}$ are all inside the unit circle. Therefore, the Lyapunov equation (42) has a unique positive-definite solution P_f, which is such that

$$P_f = \sum_{j=0}^{\infty}(\bar{\Phi}^T)^j(\bar{\Phi}^T Q\bar{\Phi} + K^T RK)\bar{\Phi}^j \quad (90)$$

From (86), (89) and (90), it can be seen that J_{DLQR} is equal to the predictive control cost (35).

References

Antropov, NN., Diakov, GA., Kim, V., Popov, GA., Pokryshkin, AI., Kazeev, MN., & Khodnenko, VP. (1999) Pulse plasma thrusters for spacecraft attitude and orbit control system. In *Proc. 26th International Electric Propulsion Conference*, Kitakyushu, Japan, pp. 1129–1135

Arntzen, B., & Maksimovic, D. (1998). Switched-capacitor DC/DC converters with resonant gate drive. *IEEE Transactions on Power Electronics*, *13*(5), 892–902.

Benmiloud, M., Benalia, A., Djemai, M., & Defoort, M. (2019). On the local stabilization of hybrid limit cycles in switched affine systems. *IEEE Transactions on Automatic Control*, *64*(2), 841–846.

Bernstein, D. S. (2009). *Matrix mathematics*. Princeton: Princeton University Press.

Cantrell, C. D. (2000). *Modern mathematical methods for physicists and engineers*. Cambridge: Cambridge University Press.

Egerstedt, M., Wardi, Y., Delmotte, F. (2003) Optimal control of switching times in switched dynamical systems. In *Proc. 42nd IEEE international conference on decision and control*, Maui, USA, pp 2138–2143.

Ferrari-Trecate, G., Gallestey, E., Letizia, P., Spedicato, M., Morari, M., & Antoine, M. (2004). Modeling and control of co-generation power plants: A hybrid system approach. *IEEE Transactions on Control Systems Technology*, *12*(5), 694–705.

Gilbert, E. G., & Tan, K. T. (1991). Linear systems with state and control constraints: The theory and application of maximal output admissible sets. *IEEE Transactions on Automatic Control*, *36*(9), 1008–1020.

Gustafsson, T. (1996). On the design and implementation of a rotary crane controller. *European Journal of Control*, *2*(3), 166–175.

Herceg, M., Kvasnica, M., Jones, C., & Morari, M. (2013) Multi-parametric toolbox 3.0. In *Proc. European control conference*, Zürich, Switzerland, pp. 502–510,http://control.ee.ethz.ch/~mpt.

Kienitz, K. (2006). Attitude stabilization with actuators subject to switching restrictions: An approach via exact relay control methods. *IEEE Transactions on Aerospace and Electronic Systems*, *42*(4), 1485–1492.

Kienitz, K. H., & Bals, J. (2005). Pulse modulation for attitude control with thrusters subject to switching restrictions. *Aerospace Science and Technology*, *9*(7), 635–640.

Kirk, D. E. (2004). *Optimal control theory: An introduction*. Mineola: Dover Publications.

Larsen, G. K. H., van Foreest, N. D., & Scherpen, J. M. A. (2013). Distributed control of the power supply-demand balance. *IEEE Transactions on Smart Grid*, *4*(2), 828–836.

Larsen, G. K. H., van Foreest, N. D., & Scherpen, J. M. A. (2014). Distributed MPC applied to a network of households with micro-

CHP and heat storage. *IEEE Transactions on Smart Grid*, *5*(4), 2106–2114.

Lewis, F. L., & Syrmos, V. L. (1995). *Optimal control* (2nd ed.). New York: Wiley.

Liu, C., Loxton, R., & Teo, K. L. (2014). Switching time and parameter optimization in nonlinear switched systems with multiple time-delays. *Journal of Optimization Theory and Applications*, *163*(3), 957–988.

Loxton, R., Teo, K., Rehbock, V., & Ling, W. (2009). Optimal switching instants for a switched-capacitor DC/DC power converter. *Automatica*, *45*(4), 973–980.

Maciejowski, J. (2002). *Predictive control with constraints*. Upper Saddle River: Prentice Hall.

Marcolino, MH. (2018). Stabilization of periodic trajectories through receding horizon optimization of switching times. PhD thesis, Instituto Tecnológico de Aeronáutica, Brazil.

Marcolino, M. H., Galvão, R. K. H., Kienitz, K. H., & Vieira, M. S. (2017). Determination of periodic trajectories of dynamic systems subject to switching input constraints. *Journal of Optimization Theory and Applications*, *175*(3), 848–864.

Parisio, A., Rikos, E., & Glielmo, L. (2014). A model predictive control approach to microgrid operation optimization. *IEEE Transactions on Control Systems Technology*, *22*(5), 1813–1827.

Patino, D., Riedinger, P., Ruiz, F. (2010) A predictive control approach for DC–DC power converters and cyclic switched systems. In *Proc. IEEE international conference on industrial technology*, pp 1259–1264.

Rom, H., & Gany, A. (1992). Thrust control of hydrazine rocket motors by means of pulse width modulation. *Acta Astronautica*, *26*(5), 313–316.

Rossi, F. Q., Galvão, R. K. H., Teixeira, M. C. M., & Assunção, E. (2019). Direct design of controllers using complementary state and state-derivative feedback. *Journal of Control, Automation and Electrical Systems*, *30*(2), 181–193.

Rossiter, J. A. (2003). *Model-based predictive control*. Boca Raton: CRC Press.

Stellato, B., Ober-Blobaum, S., & Goulart, P. J. (2017). Second-order switching time optimization for switched dynamical systems. *IEEE Transactions on Automatic Control*, *62*(10), 5407–5414.

Sun, Z., Tian, Y., & Wang, J. (2017). A novel projected fletcher-reeves conjugate gradient approach for finite-time optimal robust controller of linear constraints optimization problem: Application to bipedal walking robots. *Optimal Control Applications and Methods*, *39*(1), 130–159.

Vieira, M. (2013). Predictive control of systems with actuators subject to switching time constraints (in Portuguese). PhD thesis, Instituto Tecnológico de Aeronáutica, Brazil.

Vieira, MS., Galvão, RKH., Kienitz, KH. (2011) Attitude stabilization with actuators subject to switching-time constraints using explicit MPC. In *Proc. IEEE aerospace conference*.

Wu, X., Zhang, K., & Sun, C. (2013). Parameter tuning of multi-proportional-integral-derivative controllers based on optimal switching algorithms. *Journal of Optimization Theory and Applications*, *159*(2), 454–472.

Xu, X., & Antsaklis, P. (2004). Optimal control of switched systems based on parameterization of the switching instants. *IEEE Transactions on Automatic Control*, *49*(1), 2–16.